

pubs.acs.org/acscatalysis Research Article

CO₂ Reduction on Copper's Twin Boundary

Can Tang, Jianjian Shi, Xiaowan Bai, Anqi Hu, Ningning Xuan, Yawei Yue, Tong Ye, Bing Liu, Pengxiang Li, Peiyuan Zhuang, Jianfeng Shen, Yuanyue Liu,* and Zhengzong Sun*



Cite This: ACS Catal. 2020, 10, 2026–2032



Read Online

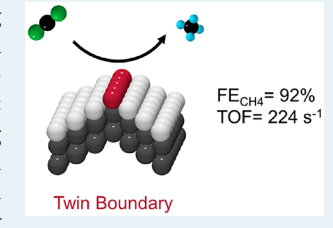
ACCESS

Metrics & More



SI Supporting Information

ABSTRACT: Electrocatalysts are evolving toward chemically tunable atomic structures, among which the catalyst engineering from a defect perspective represents one of the mainstream technical genres. However, most defects cannot be purified or their numbers gauged, making them too complex to explore the hidden catalytic mechanism. A twin boundary, with well-defined symmetric structure and high electrocatalytic activity, is an elegant one-dimensional model catalyst in pursuing such studies. Here on polished Cu electrodes, we successfully synthesized a series of copper twin boundaries, whose density ranges from 0 to 10⁵ cm⁻¹. The CH₄ turnover frequency on the twin boundary atoms is 3 orders higher than that on the plane atoms, and the local partial current density reaches 1294 mA cm⁻², with an intrinsic Faradaic efficiency of 92%. An intermediate experiment and



density functional theory studies confirm the twin boundary's advantage in converting the absorbed CO* into CH₄.

KEYWORDS: twin boundary, CO2 reduction, one-dimensional catalyst, intrinsic activity, copper, methane

INTRODUCTION

In pursuing the optimal catalyst for electrochemical CO₂ reduction reactions (CO₂RR), the catalyst's efficiency and catalytic mechanism are considered to be the golden standards for the chemical selection. Two prominent routes have been adopted in recent studies: defect engineering and dimension engineering. 1-17 The first route focuses on different types of defects, such as heteroatoms, 1,2 vacancies, 3,4 edges, 5 phase boundaries, 6,7 twin boundaries (TBs),8 and grain boundaries (GBs), 9,10 associated with their variable surface strains, 2 coordination numbers, 11 and electronic structures. 3,4,12 Regardless of the alluring efficiency, a limited mechanism has been extracted from defect-related studies. In most cases, we heavily rely on theoretical calculations to explain the possible mechanism.⁵ The major experimental challenge is to distinguish one defect effect from the others. Nevertheless, defects are hard to uniformly synthesize and their density control is still troublesome and immature in chemistry. 10

Dimension engineering is another route to tailor the catalyst. By reducing a bulk material's dimension from a three-dimensional (3D) structure down to two-dimensional (2D), 13,14 one-dimensional 1,8,15,16 (1D), or zero-dimensional (0D) 7 nanostructures, we not only open the door to precisely control the catalyst's geometry but also create more bizarre electronic structures through quantum confinement. Specifically, a 1D catalyst, composed of a single string of individual atoms, should be the thinnest catalyst existing in theory. However, in real circumstances, most 1D catalyst diameters surpass one atomic width, such as in nanowires, nanotubes, and GBs, 9,10 due to their insurmountable formation energy. The truly 1D and single atomic string structure only rarely exists on some crystal step edges and TBs, supported or stabilized by adjacent crystal lattices.

In comparison with the crystal step edges, which usually experience continuously dynamic dissolution and reconstruction during reactions, ²⁰ TB is one of the most stable and well-defined defects, existing in most metallic CO₂RR catalysts, such as Au and Cu. ⁸⁻¹⁰ In a face-centered-cubic (fcc) structure, the close-packed arrangements at TB build low interfacial energy, which endow the nanotwinned Cu (Nt-Cu) structure with exceptional mechanical strength, electrical conductivity, and enhanced thermal stability over other 1D catalysts such as GBs. ^{21,22} Moreover, the exposed TB atoms have a monopoly population in a chemically identical arrangement, which sets up a clean and succinct model for the following CO₂RR studies.

RESULTS AND DISCUSSION

Highly dense TBs were prepared by means of pulsed electrochemical deposition. 22 Typically, nanotwinned copper with the most probable twin width of 16 nm (Nt-16) was prepared from a 0.5 M CuSO_4 solution. The twin structure was confirmed with high-resolution transmission electron microscopy (HR-TEM) and selected area electron diffraction (SAED) methods. In a randomly selected observation area under TEM, parallel lines of TBs are displayed in Figure 1a. In copper's fcc crystal structure, TB is the mirror plane along the $\langle111\rangle$ directions, reversing the normal stacking order of (111) planes, forming an ABCAC_TB_TA_T stacking sequence. The atomic structure shows a symmetrical lattice arrangement

Received: September 5, 2019 Revised: December 31, 2019 Published: January 8, 2020



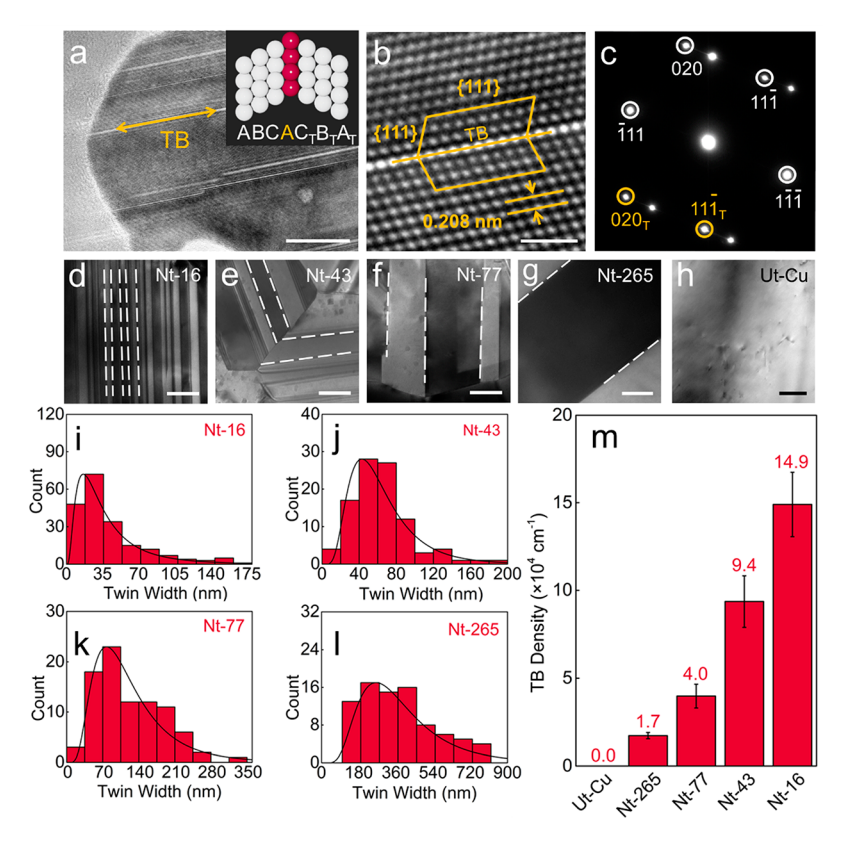


Figure 1. Copper catalysts with controllable TB density. (a) TEM image of TB assembly (inset: schematic structure of copper TB, where the red atoms represent TB atoms while the white atoms represent Cu (111) atoms). Scale bar: 10 nm. (b) Atomic structure of a representative TB in HR-TEM. Scale bar: 1 nm. The Burgers circuit is marked with two rhomboids, sharing a same side at TB. (c) The typical SAED pattern of TB. The white circles label matrix diffraction spots, while the yellow circles label twin spots. (d-h) TEM images of Nt-16, Nt-43, Nt-77, Nt-265, and Ut-Cu, respectively. The white dashed lines marked the typical TBs. Scale bar: 100 nm. (i-l) Twin width distribution histograms of Nt-16, Nt- 43, Nt-77, and Nt-265, respectively. (m) TB density statistical histogram.

mirrored by the TB (Figure 1b). In parallel with TB, the interplanar spacing is 0.208 nm, consistent with the Cu (111) plane distance. In the labeled Burgers circuit, the Burgers vector is zero, which indicates a perfect lattice structure without dislocation in this TB. The SAED image in Figure 1c shows two sets of diffraction patterns, in which the (020) and (111) spots are mirrored with $(020)_T$ and $(111)_T$ separated by (111) TB, suggesting a typical coherent TB pattern. Ideally, coherent TB is a stable 2D atomic plane embedded in the bulk crystal. Its exposed edge serves as monatomic 1D active centers in catalytic reactions.

In order to control the TB density, we annealed Nt-16 at 300, 400, and 500 °C for 3 h to obtain a series of nanotwinned Cu, named Nt-43, Nt-77, and Nt-265 (the numbers represent the most probable twin width), respectively. The untwinned Cu (Ut-Cu) was prepared by annealing Cu foil under a H₂ atmosphere at 1000 °C for 0.5 h. As the annealing temperature increases, the TB density decreases notably, as shown in Figure 1d-h. In Figure 1i-m, the quantitative analysis of the twin width and the TB density was acquired from statistical measurements in TEM images (Figures S1 and S2). In the sample Nt-16, the prominent twin width is \sim 16 nm. The corresponding TB density reaches 1.49×10^5 cm⁻¹, equivalent to a 1.49 km long TB across a 1 cm² area. After the annealing treatments at 300, 400, and 500 °C, Nt-43, Nt-77 and Nt-265 feature the most populated twin widths of 43, 77, and 265 nm, respectively. Their corresponding TB densities are 9.4×10^4 , 4.0×10^4 , and 1.7×10^4 cm⁻¹, respectively. In

comparison with these nanotwinned samples, we observed almost zero TB in Ut-Cu.

As shown by scanning electron microscopy (SEM) (Figure S3), the freshly prepared nanotwinned samples are rough with many "ridges" and "valleys" despite their similar facet orientation. In order to eliminate the roughness effect and remove the surface contamination and oxide, we electrochemically polished the Cu electrode before any electrochemical measurement (Supporting Information). The polished electrode surface got much smoother with a roughness of ~21 nm (Figure S4), and its electrochemically active surface area (EASA) was quantified from cyclic voltammetry (CV) with varied scan rates. All polished electrode samples show a similar roughness factor of ~2.9 (Figure S5). Different catalyst facets will display significantly varied activity. Therefore, we used Xray diffraction (XRD) to distinguish the main crystal facets. Among all Cu samples, the dominated facets are low-index (111) and (200), with their combination exceeding 98% (Figure S6). By eliminating the uncertainty from the surface roughness and crystal facet, we controllably synthesized nanotwinned Cu catalysts, with different TB densities and atomically thin 1D active centers, which can serve as a welldefined model catalyst to study the TB's activity in the

For an electrocatalyst, an extraordinary conductivity is a prerequisite for high catalytic activity. Therefore, we used conductive atomic force microscopy (cAFM) to explore the conductivity difference between TB and plane. In the cAFM

mapping image (Figure 2a), the white and parallel lines are consistent with TBs in its corresponding optical and SEM

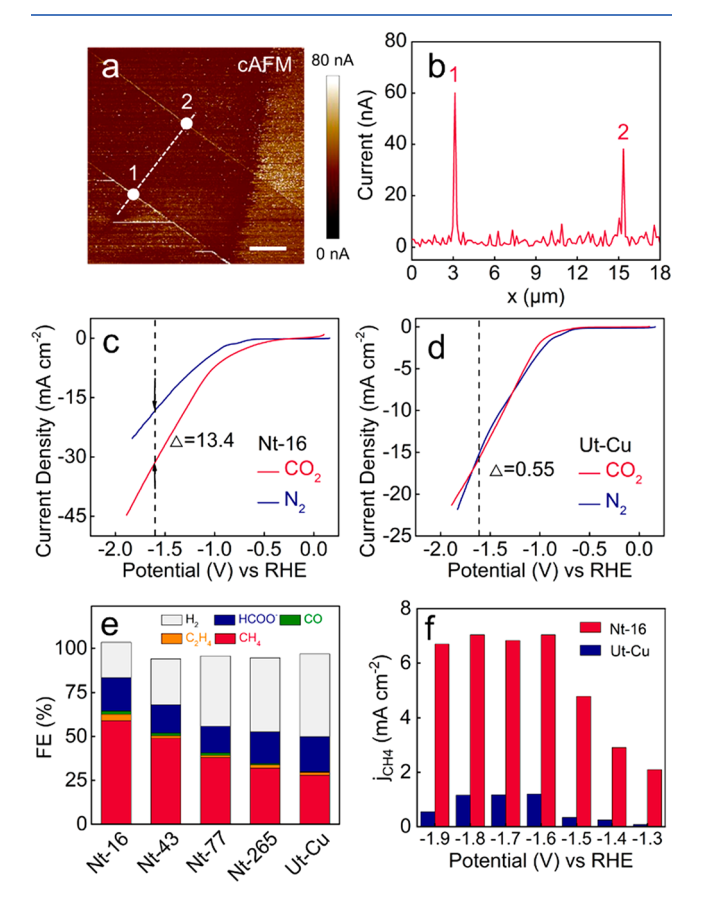


Figure 2. Electrochemical difference between nanotwinned and untwinned Cu in CO₂RR. (a) cAFM image on the TB and plane. Scale bar: 5 μ m. (b) Current profile along the dashed line in (a). Peaks 1 and 2 correspond to point 1 and 2 in (a). Linear sweeping voltammetry curves obtained on (c) Nt-16 and (d) Ut-Cu in N₂-saturated and CO₂-saturated electrolyte. (e) CO₂RR product distributions for Nt-16, Nt-43, Nt-77, Nt-265, and Ut-Cu at -1.6 V. (f) j_{CH4} values under different applied cathode voltages in CO₂-saturated solution. All electrochemical measurements were carried out in 0.2 M KHCO₃ solution at 273 K.

images (Figure S7). At typical TBs, we observed dramatic current increases (Figure 2b and Figure S8), which indicates that charges tend to transfer from TB than from the plane. This can be attributed to the fact that the undersaturated structure of TB could more easily accumulate charges and have a preferable potential to draw current.²³ Although the physical conductivity is not equivalent to chemical selectivity, the high current at TBs implies potential application in electrocatalysis.

The difference in CO_2RR between Nt-16 and Ut-Cu was first compared with linear sweeping voltammetry (LSV) (Figure 2c,d). It is commonly known that, in N₂-saturated solution, the cathodic current mainly comes from the hydrogen evolution reaction (HER), but in CO_2 -saturated solution, the HER and CO_2RR collectively contribute to the cathodic current. For Nt-16, we observed a clear current density enhancement in CO_2 -saturated solution in comparison with the N₂-saturated solution. The current density difference at -1.6 V (vs RHE) is $\sim 13.4 \text{ mA cm}^{-2}$. For Ut-Cu, these two LSV curves nearly overlap, with only 0.55 mA cm⁻² difference at the same cathode potential. The larger current density

difference for Nt-16 suggests that it could be a more efficient electrocatalyst for the CO₂RR than Ut-Cu.

To further investigate the CO2RR of nanotwinned and untwinned catalysts, their gas and liquid cathodic products were collected and analyzed by gas chromatography (GC) and ¹H nuclear magnetic resonance (NMR) (Figure S9). The primary cathodic products at −1.6 V are H₂, CH₄, CO, C₂H₄, and HCOO⁻, and their quantitative Faradaic efficiencies (FEs) are summarized in Figure 2e and Table S1. For Ut-Cu, H2 dominates the consumption of the electrons with an FEH2. value of 47%. All of the nanotwinned Cu catalysts demonstrate smaller FE_{H2} values in comparison to Ut-Cu. Particularly, the FE_{H2} value of Nt-16 is 20% and the combined FEs of CO_2 reduction (FE_{CO2}) are as high as 84%, with CH₄ as the principal product. The FE_{CH4} value of Nt-16 peaks at -1.6 V and reaches 59% (Figure S10). In Figure 2f, Nt-16 is leading Ut-Cu in the partial current density of CH_4 (j_{CH4}), and the corresponding j_{CH4} value also reaches its maximum of 7.04 mA cm^{-2} at -1.6 V. After 12 h of reaction, even nanoscaled twins remained stable and showed little change in their morphology (Figures S11 and S12). Meanwhile, as the TB distributes evenly at a different depth profile of nanotwinned Cu, we can regenerate the catalyst by polishing for several seconds, and the Nt-16 FE_{CH4} and j_{CH4} values barely fluctuate, as shown in

Since CH_4 is the major product of the CO_2RR for TB-rich copper catalysts, the correlation between the CH_4 activity and TB density was therefore studied. In order to exclude the facet effect, we measured the CO_2RR performance on Cu samples with single facets of (111) and (100), which are the main facets in our system. In terms of CH_4 production, (111), (100), and Ut-Cu showed similar activities (Figure S14). In comparison to Nt-16, the j_{CH4} variation at -1.6 V caused by facet differences is calculated to be less than 4%. In Figure 3a, the FE_{CH4} value is highly dependent on the TB density. As the

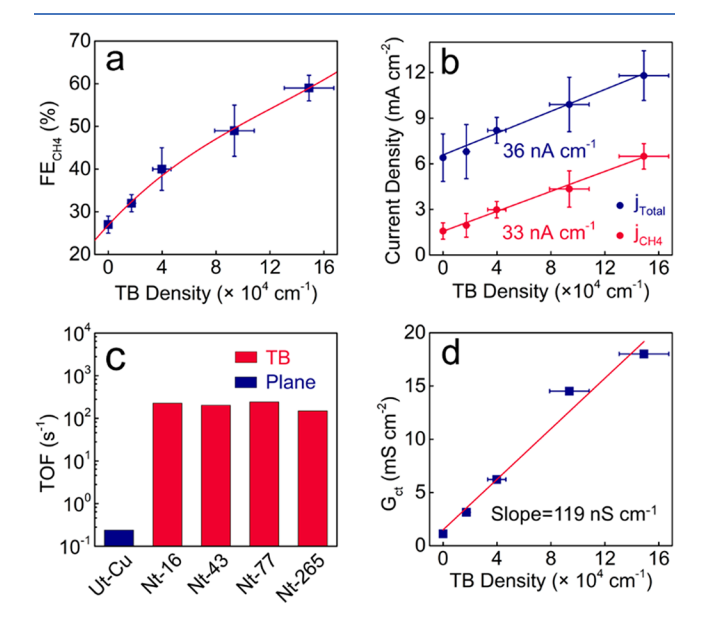


Figure 3. Linear correlation between TB density and CO_2RR . (a) Correlation between TB density and FE_{CH4} . (b) Linear relation of j or j_{CH4} versus TB density. (c) TOF histogram for CH_4 on TB (red) and plane (blue) atoms. The electrochemical measurements of (a)–(c) were performed at -1.6 V. (d) Linear relationship between G_{ct} and TB density.

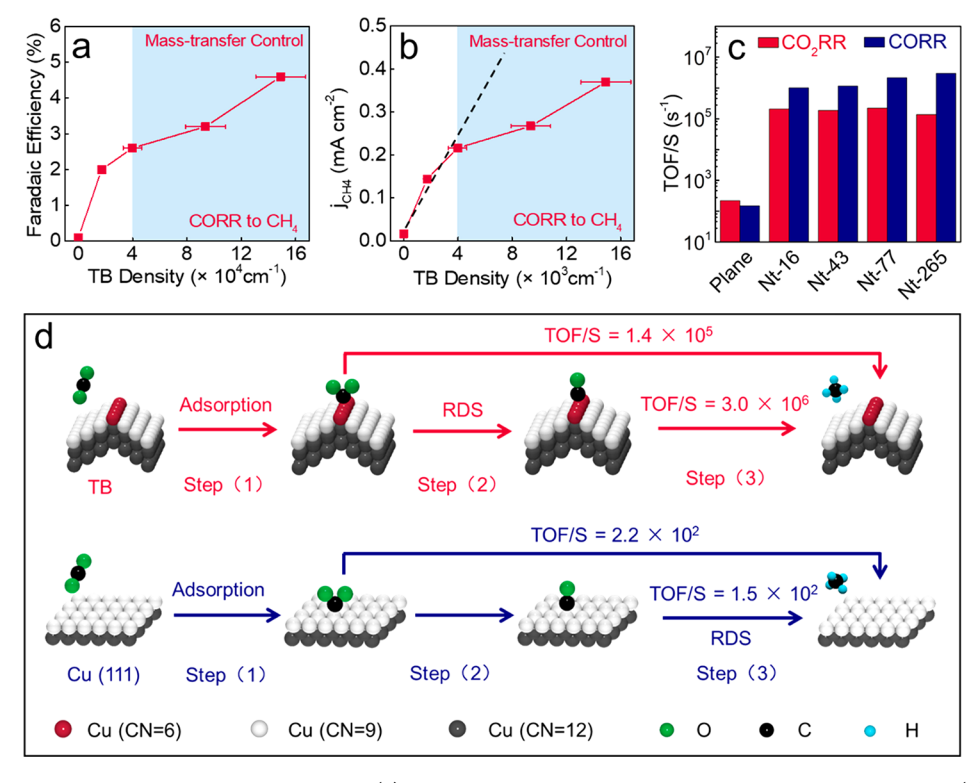


Figure 4. Exploring the rate-determining step with CORR. (a) Correlation between FE_{CH4} of the CORR and TB density. (b) j_{CH4} of the CORR facilitated by TBs. The blue shaded areas in (a) and (b) mark the reaction rate controlled by a mass-transfer process. The black dashed line in (b) represents the extrapolated linear correlation between j_{CH4} and TB density, without the mass-transfer limit of CO. (c) Solubility-corrected TOF values for the CO₂RR and CORR at plane and TB atoms (Nt-16, Nt-43, Nt-77, and Nt-265) at -1.6 V. (d) Proposed mechanism of the CO₂RR to CH₄ at TB and plane atoms. The red, white, and gray atoms represent Cu atoms with CNs of 6, 9, and 12, respectively. The green, black, and blue atoms represent oxygen, carbon, and hydrogen atoms, respectively.

TB density increases from 0 to 1.49×10^5 cm⁻¹, the FE_{CH4} value progressively climbs from 27% to 59% at -1.6 V. As shown in Figure 3b, the j_{CH4} and j_{Total} values exhibit a linear relationship with the TB density, which can be fitted as the functions

$$j_{\text{Total}} = k \times \text{TB density} + b$$
 (1)

$$j_{\text{CH4}} = k_{\text{CH4}} \times \text{TB density} + b'$$
 (2)

where the slopes ($k_{\rm CH4}$ and k) represent the current density per cm of TB and the intercepts (b and b') are current density contributed from the non-TB plane area. The intrinsic FE_{CH4} value for TB atoms can be acquired from the ratio between $k_{\rm CH4}$ (33 nA cm⁻¹) and k (36 nA cm⁻¹), which is 92%. In contrast, the other product slopes are much smaller values (Figure S15 and Table S2), suggesting their weak correlation with TB density. By assuming a monatomic 1D TB width equaling 0.255 nm, the calculated local $j_{\rm CH4}$ value at TBs is as high as 1294 mA cm⁻². This is theoretically the maximum $j_{\rm CH4}$ that a flat Cu electrode can accomplish, covered solely with TBs.

It is worth noting that the atomic density of TB in Nt-16 is \sim 9.71 \times 10⁻¹² mol cm⁻², and its corresponding atomic percentage is only \sim 0.33%, which are still much lower than those of the plane atoms (Figure S16 and Table S3). Yet in such a small amount, the j_{CH4} value from Nt-16 overtakes that of the plane atom by 310%. This implies that the TB atoms are much more active than the low-index plane atoms. Hereby, we calculated the CH₄ turnover frequency (TOF) of TB and plane atoms (Figure 3c and Table S4). All of the TOF calculations

were corrected with a roughness factor of 2.9, and the plane atom's contribution was subtracted from the TOF of TB. The detailed calculation method and results are shown in the Supporting Information and Table S4. The TOF value at the plane atom is $\sim 0.24 \text{ s}^{-1}$, which is 3 orders lower than that of the TB atom. The calculated TOFs on Nt-16, Nt-43, Nt-77, and Nt-265 are 226, 203, 242, and 149 s⁻¹, respectively. After fitting the EASA-normalized j_{CH4} versus TB atomic density with a linear plot, we acquired the TOF of TB equaling 224 s⁻¹ from the slope in Figure S17. Our TB Cu atom represents the most efficient catalytic center in up to date studies^{9,5,24–34} (Figure S18 and Table S5), exhibiting ~1 order higher TOF than the state of the art single-atom catalysts.²⁹ Given that a few GBs existed in our samples (Figure S19), we synthesized Cu with defects dominated by GBs (GB-Cu) by direct-current deposition³⁵ to evaluate the GB effect in the CO₂RR (Figure S20). The TB density in GB-Cu is only 1.34×10^4 cm⁻¹, even less than that in Nt-265. However, the GB density in GB-Cu $(1.02 \times 10^5 \text{ cm}^{-1})$ is ~4 times higher than that in Nt-16 (2.19 \times 10⁴ cm⁻¹). Despite a great number of GBs, j_{CH4} of GB-Cu $(2.74 \text{ mA cm}^{-2})$ at -1.6 V is only slightly higher than that of Ut-Cu. It seems that GB-Cu ($FE_{CH4} = 25\%$) is less selective to CH₄. If we consider a much lower GB density in our samples, the GB's contribution to j_{CH4} is actually lower than 5% (Figure

The much faster TOF at TB atoms implies that the kinetics of the CO_2 reduction to CH_4 process is strikingly swift on TBs. In general, the reaction rate for an electrochemical reaction is highly dependent on the interfacial charge-transfer process. Close to the equilibrium potential, the electrochemical

impedance spectroscopy (EIS) was taken to study the TB charge-transfer capability. On the basis of the Nyquist plots (Figure S22), the charge-transfer conductance ($G_{\rm ct}$) can be deducted from the reciprocal of charge-transfer resistance ($R_{\rm ct}$). As shown in Figure 3d, the $G_{\rm ct}$ value increases linearly with the TB density, with a slope of 119 nS cm⁻¹. Although the measured $G_{\rm ct}$ contains the contribution from both the HER and CO₂RR, the linear correlation between $G_{\rm ct}$ and TB density reflects that TB is the major catalytic center which demonstrates a strong capability of transferring electrons in the electrocatalysis process. In Figure S23, the Tafel slopes for Nt-16 and Ut-Cu are 130 and 261 mV dec⁻¹, respectively, further indicating a kinetic preference on TB.

CO* is regarded as one of the critical intermediates in the CO₂RR before forming CH₄.³⁶⁻³⁸ Therefore, we performed the CO reduction reaction (CORR) in CO-saturated 0.2 M KHCO3 to investigate the role of TB role in CO* hydrogenation. As shown in Figure 4a, Ut-Cu only exhibits a negligible FE_{CH4} for the CORR of 0.1%. In contrast, Nt-16 has the highest FE_{CH4} value of 4.6%, a 45-fold increase. Meanwhile, the j_{CH4} value of the CORR in Figure 4b increases by 23 times, from 0.016 (Ut-Cu) to 0.37 (Nt-16) mA cm⁻², despite their similar HER capabilities shown in Figure S24. We did not observe a linear correlation between j_{CH4} and TB density as in the CO₂RR process. In the region of low TB density, the j_{CH4} value still follows a linear correlation along the black dashed line in Figure 4b with TB density. As the TB density increases, the current density starts to deviate from the dashed line. This could be attributed to a lower amount of solubility of CO in comparison to CO₂ in the electrolyte solution. Therefore, the growth of j_{CH4} in the CORR is limited by the mass transfer of CO. The corresponding TOFs for the CORR at TB and plane atoms are shown in Figure S25 and Table S6. The TOF of TB on Nt-16 is 22 s⁻¹, which is 4 orders of magnitude faster than that at plane atoms, confirming the fast CO* hydrogenation on

Since the TOFs for CO_2RR and CORR (TOF_{CO2} and TOF_{CO}) were obtained without considering the different CO_2 and CO solubilities (S_{CO2} and S_{CO} , mole fraction), we used TOF_{CO2}/S_{CO2} and TOF_{CO}/S_{CO} to represent the corrected rates. As illustrated in Figure 4c, all of the TBs in the nanotwinned samples show a higher TOF_{CO}/S_{CO} in comparison to TOF_{CO2}/S_{CO2} . Sample Nt-265 is only kinetically controlled in both the CO_2RR and CORR reactions. The corresponding value of TOF_{CO}/S_{CO} is ~23 times of that of TOF_{CO2}/S_{CO2} , which is the largest difference between these two corrected rates. Plane atoms in Ut-Cu demonstrate a small margin in the corrected values.

On the basis of our experimental results on TOF/S, we deduced the possible CO₂RR mechanism on TB and plane atoms, as shown in Figure 4d. It is generally accepted that CO₂ transformation to CH₄ on Cu usually takes three steps:^{36–39} (1) the adsorption of CO₂, (2) the intermediate CO* formation, and (3) the CO* hydrogenation. Among the three steps, steps 2 and 3 are regarded as the key steps, which involve an electron-transfer process. For TB, the CORR rate (step 3) is much higher than that of the CO₂RR (step 2 + step 3). According to the rate relationship in a consecutive reaction, step 2 is determined to be its the rate-determining step (RDS). Once CO* forms, it immediately transforms into CH₄ on TB, giving rise to the high FE_{CH4} value. For plane atoms, step 3 is as fast as the combined CO₂RR steps (step 2 + step 3), which suggests that step 3 is more likely to be the RDS, consistent

with former studies.^{35–38} As the CO* cannot be easily hydrogenated on plane atoms, Ut-Cu is less selective to CH₄.

In this proposed reaction scheme, the TB coordination number (CN) is highly unsaturated (ideally CN = 6), which is smaller than the plane's 9 and the saturated CN's 12. This small CN could endow TB with enhanced catalytic activity in both step 2 and step 3. Further theoretical study by the density functional theory (DFT) reveals how the low-coordinated structure enhances the CH_4 production (Figure 5). DFT

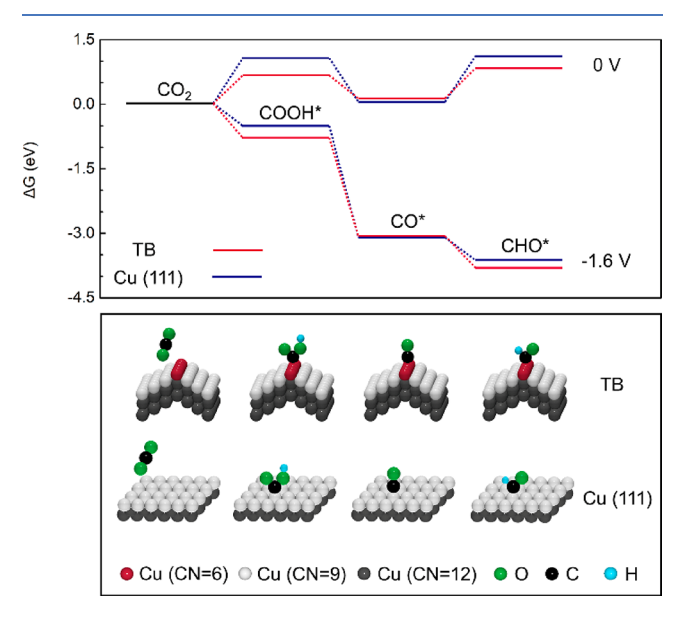


Figure 5. DFT calculation of the CO_2 reduction to CH_4 at TBs and Cu (111) facet. The schematic diagram contains the intermediate structures on TB and Cu (111) corresponding to the DFT calculations. The red, white, and gray atoms represent Cu atoms with CNs of 6, 9, and 12, respectively. The green, black, and blue atoms represent oxygen, carbon, and hydrogen atoms, respectively.

calculations 40,41 indicate that COOH* and CHO* are the critical intermediates for $\text{CO}_2^* \to \text{CO}^*$ and $\text{CO}^* \to \text{CH}_4$, respectively. At U = 0 V, the formation of COOH* and CHO* is endothermic on both catalysts. The production of CH₄ at TB is more favorable than that at Cu facet, for the free energies of COOH* and CHO* at TBs are stabilized by -0.37 and -0.27 eV, respectively, in comparison with Cu (111). The more detailed reaction pathways are shown in Figure S26. In addition, the hydrogenation of CH₃O* to CH₄ can also support this because the $CH_3O^* + H^+ + e^- \rightarrow O^* + CH_4$ elementary reaction at TBs (-0.74 eV) can release more energy than the Cu (111) surface (-0.69 eV). After the effect of solvation is considered, the free energies of nearly all intermediates decrease, but a similar trend is also observed in Figure S27. At U = 1.6 V, although all elementary reactions are exothermic on both catalysts, the hydrogenation of CO* to form CHO* at TBs is still more exothermic. The above results show that the presence of TB can increase the production of CH₄, in agreement with our experiments.

CONCLUSION

In conclusion, we quantitatively synthesized the thinnest 1D active sites, the TB, with a controllable density from 0 to 10^5 cm $^{-1}$. On the basis of the linear correlation between CO $_2$ reduction activity and the TB density, we found an extreme local $j_{\rm CH4}$ of 1294 mA cm $^{-2}$ on TB, with an intrinsic CH $_4$

selectivity of 92%. With a further intermediate CORR study, the TB atoms are 10^4 faster than the plane atoms in CO* protonation, coinciding with the DFT calculation. We believe our quantitative TB model catalyst study could be extended to other $\rm CO_2RR$ metal catalysts, such as Ag and Au, and open a new door for future rational catalyst design.

ASSOCIATED CONTENT

Supporting Information

The Supporting Information is available free of charge at https://pubs.acs.org/doi/10.1021/acscatal.9b03814.

Experimental details, ¹H NMR and XRD spectra, SEM and TEM images, GC data, current densities and FEs, active site tests, comparison of CO₂RR performance, and reaction pathways (PDF)

AUTHOR INFORMATION

Corresponding Authors

Yuanyue Liu — The University of Texas at Austin, Austin, Texas; ⊚ orcid.org/0000-0002-5880-8649;

Email: yuanyue.liu@austin.utexas.edu

Zhengzong Sun − Fudan University, Shanghai, People's Republic of China; oorcid.org/0000-0002-3710-4001; Email: zhengzong sun@fudan.edu.cn

Other Authors

Can Tang – Fudan University, Shanghai, People's Republic of China

Jianjian Shi – The University of Texas at Austin, Austin, Texas

Xiaowan Bai — The University of Texas at Austin, Austin, Texas

Anqi Hu – Fudan University, Shanghai, People's Republic of China

Ningning Xuan – Fudan University, Shanghai, People's Republic of China

Yawei Yue - Fuzhou University, Fuzhou, People's Republic of China

Tong Ye – Fudan University, Shanghai, People's Republic of China

Bing Liu – Fudan University, Shanghai, People's Republic of China

Pengxiang Li – Fudan University, Shanghai, People's Republic of China

Peiyuan Zhuang – Fudan University, Shanghai, People's Republic of China

Jianfeng Shen – Fudan University, Shanghai, People's Republic of China

Complete contact information is available at: https://pubs.acs.org/10.1021/acscatal.9b03814

Author Contributions

C.T. and Z.S. conceived the project, analyzed the data, and wrote the paper. C.T. synthesized the samples. C.T., Y.Y., and B.L. performed the gas products evaluation. C.T. and T.Y. analyzed the liquid products. C.T. and A.H. ran the TEM and XRD tests. N.X. performed cAFM. P.L. and P.Z. ran the SEM test. Y.L., X.B., and J.S. performed the DFT calculations. J.S. gave advice on the paper. All authors read and commented on the manuscript.

Notes

The authors declare no competing financial interest.

ACKNOWLEDGMENTS

The authors are grateful for the financial support from the National Natural Science Foundation of China (21771040), the National Key Research and Development Program of China (2017YFA0207303, 2016YFA0203900), and the 1000 Plan Program for Young Talents. Y.L. acknowledges the support by the National Science Foundation (Grant No. 1900039) and the Welch Foundation (Grant No. F-1959-20180324). This work used computational resources at (1) National Renewable Energy Lab (spondored by the DOE's Office of EERE), (2) the Extreme Science and Engineering Discovery Environment (XSEDE) through allocation TG-CHE190065, (3) the Center for Nanoscale Materials (a DOE Office of Science user facility supported under Contract No. DE-AC02-06CH11357) at Argonne National Lab, and (4) the Center for Nanophase Materials Science (a DOE Office of Science user facility) at Oak Ridge National Lab.

REFERENCES

- (1) Sharma, P. P.; Wu, J.; Yadav, R. M.; Liu, M.; Wright, C. J.; Tiwary, C. S.; Yakobson, B. I.; Lou, J.; Ajayan, P. M.; Zhou, X.-D. Nitrogen-doped carbon nanotube arrays for high-efficiency electrochemical reduction of CO₂: on the understanding of defects, defect density, and selectivity. *Angew. Chem., Int. Ed.* **2015**, *54*, 13701–13705.
- (2) Clark, E. L.; Hahn, C.; Jaramillo, T. F.; Bell, A. T. Electrochemical CO_2 reduction over compressively strained CuAg surface alloys with enhanced multi-carbon oxygenate selectivity. *J. Am. Chem. Soc.* **2017**, *139*, 15848–15857.
- (3) Geng, Z.; Kong, X.; Chen, W.; Su, H.; Liu, Y.; Cai, F.; Wang, G.; Zeng, J. Oxygen vacancies in ZnO nanosheets enhance $\rm CO_2$ electrochemical reduction to CO. *Angew. Chem., Int. Ed.* **2018**, 57, 6054–6059.
- (4) Gao, S.; Sun, Z.; Liu, W.; Jiao, X.; Zu, X.; Hu, Q.; Sun, Y.; Yao, T.; Zhang, W.; Wei, S.; Xie, Y. Atomic layer confined vacancies for atomic-level insights into carbon dioxide electroreduction. *Nat. Commun.* **2017**, *8*, 14503.
- (5) Abbasi, P.; Asadi, M.; Liu, C.; Sharifi-Asl, S.; Sayahpour, B.; Behranginia, A.; Zapol, P.; Shahbazian-Yassar, R.; Curtiss, L. A.; Salehi-Khojin, A. Tailoring the edge structure of molybdenum disulfide toward electrocatalytic reduction of carbon dioxide. *ACS Nano* **2017**, *11*, 453–460.
- (6) Lee, S.; Park, G.; Lee, J. Importance of Ag-Cu biphasic boundaries for selective electrochemical Reduction of ${\rm CO_2}$ to Ethanol. *ACS Catal.* **2017**, *7*, 8594–8604.
- (7) Morales-Guio, C. G.; Cave, E. R.; Nitopi, S. A.; Feaster, J. T.; Wang, L.; Kuhl, K. P.; Jackson, A.; Johnson, N. C.; Abram, D. N.; Hatsukade, T.; Hahn, C.; Jaramillo, T. F. Improved CO₂ reduction activity towards C₂+ alcohols on a tandem gold on copper electrocatalyst. *Nat. Catal.* **2018**, *1*, 764–771.
- (8) Li, Y.; Cui, F.; Ross, M. B.; Kim, D.; Sun, Y.; Yang, P. Structure-sensitive CO₂ electroreduction to hydrocarbons on ultrathin 5-fold twinned copper nanowires. *Nano Lett.* **2017**, *17*, 1312–1317.
- (9) Feng, X.; Jiang, K.; Fan, S.; Kanan, M. W. Grain-boundary-dependent CO₂ electroreduction activity. *J. Am. Chem. Soc.* **2015**, *137*, 4606–4609.
- (10) Mariano, R. G.; McKelvey, K.; White, H. S.; Kanan, M. W. Selective increase in CO_2 electroreduction activity at grain-boundary surface terminations. *Science* **2017**, 358, 1187–1192.
- (11) Wang, Y.; Han, P.; Lv, X.; Zhang, L. I.; Zheng, G. Defect and interface engineering for aqueous electrocatalytic CO₂ reduction. *Joule* **2018**, *2*, 2551–2582.

- (12) Chen, Z.; Zhang, X.; Lu, G. Overpotential for $\rm CO_2$ electroreduction lowered on strained penta-twinned Cu nanowires. *Chem. Sci.* **2015**, *6*, 6829–6835.
- (13) Gao, S.; Lin, Y.; Jiao, X.; Sun, Y.; Luo, Q.; Zhang, W.; Li, D.; Yang, J.; Xie, Y. Partially oxidized atomic cobalt layers for carbon dioxide electroreduction to liquid fuel. *Nature* **2016**, *529*, 68–71.
- (14) Lei, F.; Liu, W.; Sun, Y.; Xu, J.; Liu, K.; Liang, L.; Yao, T.; Pan, B.; Wei, S.; Xie, Y. Metallic tin quantum sheets confined in graphene toward high-efficiency carbon dioxide electroreduction. *Nat. Commun.* **2016**, *7*, 12697.
- (15) Zhu, W.; Zhang, Y.; Zhang, H.; Lv, H.; Li, Q.; Michalsky, R.; Peterson, A. A.; Sun, S. Active and selective conversion of CO₂ to CO on ultrathin Au nanowires. *J. Am. Chem. Soc.* **2014**, *136*, 16132–16135.
- (16) Ma, M.; Djanashvili, K.; Smith, W. A. Controllable hydrocarbon formation from the electrochemical reduction of CO₂ over Cu nanowire arrays. *Angew. Chem.* **2016**, *128*, *6792*–*6796*.
- (17) Wu, J.; Ma, S.; Sun, J.; Gold, J. I.; Tiwary, C.; Kim, B.; Zhu, L.; Chopra, N.; Odeh, I. N.; Vajtai, R.; Yu, A. Z.; Luo, R.; Luo, J.; Ding, G.; Kenis, P. J. A.; Ajayan, P. M. A metal-free electrocatalyst for carbon dioxide reduction to multi-carbon hydrocarbons and oxygenates. *Nat. Commun.* **2016**, *7*, 13869.
- (18) Gülseren, O.; Ercolessi, F.; Tosatti, E. Noncrystalline structures of ultrathin unsupported nanowires. *Phys. Rev. Lett.* **1998**, *80*, 3775–3778.
- (19) Wen, R.; Lahiri, A.; Azhagurajan, M.; Kobayashi, S.; Itaya, K. A new in situ optical microscope with single atomic layer resolution for observation of electrochemical dissolution of Au (111). *J. Am. Chem. Soc.* **2010**, *132*, 13657–13659.
- (20) Wilms, M.; Broekmann, P.; Kruft, M.; Stuhlmann, C.; Wandelt, K. STM investigation of step orientation and surface dynamics of Cu (111) in hydrochloric acid electrolyte. *Appl. Phys. A: Mater. Sci. Process.* 1998, 66, S473–S475.
- (21) Lu, K. Stabilizing nanostructures in metals using grain and twin boundary architectures. *Nat. Rev. Mater.* **2016**, *1*, 16019.
- (22) Lu, L.; Shen, Y.; Chen, X.; Qian, L.; Lu, K. Ultrahigh strength and high electrical conductivity in copper. *Science* **2004**, *304*, 422–426.
- (23) Yao, Z.; Song, Z.; Hao, H.; Yu, Z.; Cao, M.; Zhang, S.; Lanagan, M. T.; Liu, H. Homogeneous/inhomogeneous-structured dielectrics and their energy-storage performances. *Adv. Mater.* **2017**, 29, 1601727.
- (24) Weng, Z.; Jiang, J.; Wu, Y.; Wu, Z.; Guo, X.; Materna, K.; Liu, W.; Batista, V. S.; Brudvig, G. W.; Wang, H. Electrochemical CO_2 reduction to hydrocarbons on a heterogeneous molecular Cu catalyst in aqueous solution. *J. Am. Chem. Soc.* **2016**, *138*, 8076–8079.
- (25) Zhao, C.; Dai, X.; Yao, T.; Chen, W.; Wang, X.; Wang, J.; Yang, J.; Wei, S.; Wu, Y.; Li, Y. Ionic exchange of metal-organic frameworks to access single nickel sites for efficient electroreduction of CO₂. J. Am. Chem. Soc. **2017**, 139, 8078–8081.
- (26) Kauffman, D. R.; Thakkar, J.; Siva, R.; Matrange, C.; Ohodnicki, P. R.; Zeng, C.; Jin, R. Efficient electrochemical CO₂ conversion powered by renewable energy. *ACS Appl. Mater. Interfaces* **2015**, *7*, 15626–15632.
- (27) Lin, S.; Diercks, C. S.; Zhang, Y.-B.; Kornienko, N.; Nichols, E. M.; Zhao, Y.; Paris, A. R.; Kim, D.; Yang, P.; Yaghi, O. M.; Chang, C. J. Covalent organic frameworks comprising cobalt porphyrins for catalytic CO₂ reduction in water. *Science* **2015**, 349, 1208–1213.
- (28) Gao, D.; Zhou, H.; Wang, J.; Wang, G.; Bao, X. Pd-containing nanostructures for electrochemical CO_2 reduction reaction. *ACS Catal.* **2018**, *8*, 1510–1519.
- (29) Cheng, Y.; Zhao, S.; Johannessen, B.; Veder, J.-P.; Saunders, M.; Rowles, M. R.; Cheng, M.; Liu, C.; Chisholm, M. F.; De Marco, R.; Cheng, H.-M.; Yang, S.-Z.; Jiang, S. P. Atomically dispersed transition metals on carbon nanotubes with ultrahigh loading for selective electrochemical carbon dioxide reduction. *Adv. Mater.* **2018**, 30, 1706287.
- (30) Zhang, X.; Wu, Z.; Zhang, X.; Li, L.; Li, Y.; Xu, H.; Li, X.; Yu, X.; Zhang, Z.; Liang, Y.; Wang, H. Highly selective and active CO₂

- reduction electrocatalysts based on cobalt phthalocyanine/carbon nanotube hybrid structures. *Nat. Commun.* **2017**, *8*, 14675.
- (31) Hsieh, Y. C.; Senanayake, S. D.; Zhang, Y.; Xu, W.; Polyansky, D. E. Effect of chloride anions on the synthesis and enhanced catalytic activity of silver nanocoral electrodes for CO₂ electroreduction. *ACS Catal.* **2015**, *5*, 5349–5356.
- (32) Yang, H. B.; Hung, S.-F.; Liu, S.; Yuan, K.; Miao, S.; Zhang, L.; Huang, X.; Wang, H.-Y.; Cai, W.; Chen, R.; Gao, J.; Yang, X.; Chen, W.; Huang, Y.; Chen, H. M.; Chang, M. L.; Zhang, T.; Liu, B. Atomically dispersed Ni (I) as the active site for electrochemical CO₂ Reduction. *Nat. Energy* **2018**, *3*, 140–147.
- (33) Wang, Y.-R.; Huang, Q.; He, C.-T.; Chen, Y.; Liu, J.; Shen, F.-C.; Lan, Y.- Q. Oriented electron transmission in polyoxometalatemetalloporphyrin organic framework for highly selective electroreduction of CO₂. *Nat. Commun.* **2018**, *9*, 4466.
- (34) Pan, Y.; Lin, R.; Chen, Y.; Liu, S.; Zhu, W.; Cao, X.; Chen, W.; Wu, K.; Cheong, W.-C.; Wang, Y.; Zheng, L.; Luo, J.; Lin, Y.; Liu, Y.; Liu, C.; Li, J.; Lu, Q.; Chen, X.; Wang, D.; Peng, P.; Chen, C.; Li, Y. Design of single-atom Co-N₅ catalytic site: a robust electrocatalyst for CO₂ reduction with nearly 100% CO selectivity and remarkable stability. *J. Am. Chem. Soc.* **2018**, *140*, 4218–4221.
- (35) Lu, L.; Chen, X.; Huang, X.; Lu, K. Revealing the maximum strength in nanotwinned copper. *Science* **2009**, 323, 607–610.
- (36) Gattrell, M.; Gupta, N.; Co, A. A review of the aqueous electrochemical reduction of CO_2 to hydrocarbons at copper. *J. Electroanal. Chem.* **2006**, 594, 1–19.
- (37) Nie, X.; Esopi, M. R.; Janik, M. J.; Asthagiri, A. Selectivity of CO₂ reduction on copper electrodes: the role of the kinetics of elementary steps. *Angew. Chem., Int. Ed.* **2013**, *52*, 2459–2462.
- (38) Peterson, A. A.; Nørskov, J. K. Activity descriptors for CO_2 electroreduction to methane on transition-metal catalysts. *J. Phys. Chem. Lett.* **2012**, *3*, 251–258.
- (39) Schouten, K. J. P.; Kwon, Y.; Van der Ham, C. J. M.; Qin, Z.; Koper, M. T. M. A new mechanism for the selectivity to C_1 and C_2 species in the electrochemical reduction of carbon dioxide on copper electrodes. *Chem. Sci.* **2011**, *2*, 1902–1909.
- (40) Kohn, W.; Sham, L. J. Self-Consistent Equations Including Exchange and Correlation Effects. *Phys. Rev.* **1965**, *140*, A1133–A1138.
- (41) Peterson, A. A.; Abild-Pedersen, F.; Studt, F.; Rossmeisl, J.; Nørskov, J. K. How copper catalyzes the electroreduction of carbon dioxide into hydrocarbon fuels. *Energy Environ. Sci.* **2010**, *3*, 1311–1315.